Nano-needle strontium-substituted apatite coating enhances osteoporotic osseointegration through promoting osteogenesis and inhibiting osteoclastogenesis

Zhen Geng[a,c], Luli Ji[a,c], Zhaoyang Li[a,*], Jing Wang[a,d,**], Hongyan He[a,c], Zhenduo Cui[b], Xianjin Yang[b], Changsheng Liu[a,c,d]

[a] Key Laboratory for Ultrafine Materials of Ministry of Education, East China University of Science and Technology, Shanghai, 200237, China
[b] Tianjin Key Laboratory of Composite and Functional Materials, School of Materials Science and Engineering, Tianjin University, Tianjin, 300350, China
[c] Engineering Research Center for Biomedical Materials of the Ministry of Education, East China University of Science and Technology, Shanghai, 200237, China
[d] The State Key Laboratory of Bioreactor Engineering, East China University of Science and Technology, Shanghai, 200237, China

ARTICLE INFO

ABSTRACT

Implant loosening remains a major clinical challenge for osteoporotic patients. This is because osteoclastic bone resorption rate is higher than osteoblastic bone formation rate in the case of osteoporosis, which results in poor bone repair. Strontium (Sr) has been widely accepted as an anti-osteoporosis element. In this study, we fabricated a series of apatite and Sr-substituted apatite coatings via electrochemical deposition under different acidic conditions. The results showed that Ca and Sr exhibited different mineralization behaviors. The main mineralization products for Ca were $CaHPO_4 \cdot 2H_2O$ and $Ca_3(PO_4)_2$ with the structure changed from porous to spherical as the pH values increased. The main mineralization products for Sr were $SrHPO_4$ and $Sr_5(PO_4)_3OH$ with the structure changed from flake to needle as the pH values increased. The *in vitro* experiment demonstrated that coatings fabricated at high pH condition with the presence of Sr were favorable to MSCs adhesion, spreading, proliferation, and osteogenic differentiation. In addition, Sr-substituted apatite coatings could evidently inhibit osteoclast differentiation and fusion. Moreover, the *in vivo* study indicated that nano-needle like Sr-substituted apatite coating could suppress osteoclastic activity, improve new bone formation, and enhance bone-implant integration. This study provided a new theoretical guidance for implant coating design and the fabricated Sr-substituted coating might have potential applications for osteoporotic patients.

1. Introduction

With the acceleration of the aging population, more and more people are suffering from bone-related diseases, such as osteoarthritis (OA). Statistically, 250 million people are currently affected by OA and this number continues to rise [1]. Unfortunately, there is still no effective cure for OA. Advanced OA patients can only be alleviated by a joint replacement surgery to relieve the pain and gain mobility [2,3]. Additionally, a large proportion of advanced OA patients often suffer from osteoporosis (OP), another bone disease, which results in decreased bone repair speed and thus implant loosening [4,5]. Currently, implant loosening is still the main reason for the failure of operation, which will bring considerable mental and physical pain to patients

[6–9]. Therefore, improving bone-implant osseointegration and bonding strength, especially for the osteoporotic patients, remains a clinical challenge.

As well known, calcium-phosphorus (Ca-P) compound, also known as apatite, is the major inorganic composition of bone tissue [10]. With this regard, apatite has been widely used as bone filling material and implant coating for decades [11–13]. Previous studies have confirmed that apatite can promote *in vitro* osteoblast adhesion, spreading, proliferation, and differentiation [14–16]. In addition, numerous studies have proved that apatite coating can enhance *in vivo* bone-implant osseointegration and bonding strength [17,18]. However, apatite fails to give satisfying performance in osteoporotic patients [19]. This is mainly because apatite can't effectively reduce the overactive osteoclastic

activity in OP condition, which results in low bone growth rate.

Strontium (Sr), a necessary trace element for human, is a bone-targeting element and mainly found in the skeleton [20]. Previous studies have found that Sr could promote MSCs proliferation and osteogenic differentiation [21–23]. In addition, studies demonstrated that Sr could effectively inhibit osteoclast differentiation and osteoclastic activity [24]. Moreover, Xie et al. found that strontium and the surrounding calcium showed a synergistic effect on bone regeneration in a dose-dependent manner [25,26]. With this regard, Sr has been widely doped into various biomaterials to achieve the desired bone repair effect [27–29]. For example, Sr-doped ceramics could not only promote *in vitro* osteogenic differentiation but also inhibit osteoclast differentiation [30,31]. Moreover, Sr-doped materials could accelerate *in vivo* bone repair through suppressing osteoclast activity in osteoporotic model [32–34]. Based on this, Sr-doped apatite coating is expected to have desirable performance in osteoporotic model.

In this study, a series of apatite and Sr-substituted apatite were deposited on implant surface via electrochemical deposition method under different acidic conditions. Then, their physicochemical properties and biological performances (including *in vitro* and *in vivo*) were characterized and evaluated, respectively.

2. Materials and methods

2.1. Samples preparation

To fabricate the apatite (or Sr-substituted apatite P) coating, an electrolyte was prepared by dissolving $0.042 \ mol \ L^{-1} \ Ca(NO_3)_2 \cdot 4H_2O$ (or $Sr(NO_3)_2$) and $0.025 \ mol \ L^{-1} \ NH_4H_2PO_4$ in deionized water. Platinum was used as the anode and the pure Ti (*in vitro* section, Ti discs, Φ 20 mm $\times$ 1 mm; *in vivo* section, Ti cylinders, Φ 4 mm $\times$ 7 mm) as the cathode. Five acidic environments (pH values ranged from 3.7 to 4.9, adjusted by HCl and NaOH solutions) were chosen to explore the mineralization behavior of Ca and Sr. Electrodeposition was carried out at a stable cathodic potential of 4 V for 20 min at room temperature. After the deposition, all the samples were rinsed with ultrapure water and dried at 50 °C for 12 h. The samples are distinguished by the pH values and cations (Table 1). For example, Ti-Ca3.7 indicates that the sample prepared by $Ca(NO_3)_2 \cdot 4H_2O$ with a pH value of 3.7.

2.2. Samples characterization

Phase analysis of the obtained samples was conducted using X-ray powder diffraction (XRD). Scanning electron microscope (SEM) and Transmission electron microscopy (TEM) images were obtained on S-4800 Hitachi and JEOL JEM2100, respectively. Fourier transitioned infrared spectroscopy (FTIR, Bruker Tensor 27, Germany) was used to examine the functional groups. The thermogravimetric (TG) analysis was performed using a TGA/DSC 1 (METTLER TOLEDO, Switzerland). The atomic concentrations of the elements (Ca, Sr, and P) in the samples were quantified using an inductive coupled plasma emission spectrometer (ICP, VISTA-MPX).

2.3. In vitro section

2.3.1. MSCs adhesion, spreading, proliferation and osteogenic differentiation

After being cultured for 12 h and 3 days, MSCs actin cytoskeleton and nuclei were stained with phalloidin and DAPI, respectively. MSC adhesion was visualized and captured via the microscopy. After being cultured for 1 and 3 days, expression of integrin-related genes (including integrin α5 (ITG α5) and integrin β1 (ITG β1)) were quantified.

After being cultured for 3 and 7 days, MTT assay was performed to evaluate MSC proliferation. Alkaline phosphatase (ALP) colorimetric assay (Abcam, Cambridge, UK) was used to assess the osteogenic differentiation of MSCs. In addition, osteogenesis-related genes (including the alkaline phosphatase (ALP), runt-related transcription factor 2 (Runx2), osteocalcin (OCN), and collagen I (Col-I)) were quantified.

2.3.2. Osteoclast differentiation and activity

Bone marrow mononuclear cells (BMMCs) were obtained from two-month-old C57BL/6 mice. M-CSF (R&D, USA, 30 ng/mL) and RANKL (R&D, USA, 50 ng/mL) were used to induce the osteoclast differentiation. Osteoclastic activity was evaluated via TRAP staining kit and TRAP enzyme assay kit (Sigma-Aldrich, USA). In addition, osteoclast fusion rate and actin ring formation assays were conducted. Finally, the expression of the osteoclastogenesis-related genes, including TRAP, osteoclast-associated receptor (OSCAR), Nuclear factor of activated T-cells cytoplasmic 1 (NFATc1), and Cathepsin K, were quantified.

2.4. In vivo section

All animal procedures were performed according to guidelines approved by the East China University of Science and Technology Ethics Committee. New Zealand white rabbits (3.5–4 kg, 1 year old) were used in this study. After ovariectomy surgery for 4 months, each rabbit was implanted with two rods (distal femur for each leg). At each harvest time, X-ray and micro-CT were performed to observe the implants condition. Meanwhile, trabecular thickness (Tb·Th) and new bone volume were analyzed. The bone-implant interface observation and bone–implant contact (BIC) calculation were evaluated by hard tissue slices. Bone–implant bonding strength was evaluated by biomechanical push-in test. Histological analysis was assessed via hematoxylin/eosin (HE) and Masson's trichrome staining to investigate the new bone. TRAP staining was performed to evaluate the osteoclast activity around implant. In addition, immunohistochemical staining, including Collagen I (Col-I, Abcam) and osteocalcin (OCN, Abcam), were performed to evaluate the metabolism of new bone. (For more details, see Supplementary Information).
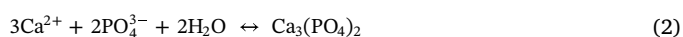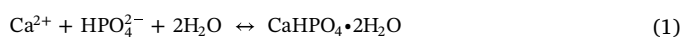
2.5. Statistical analysis

All values are presented as the means ± standard deviations. The statistical analysis was performed using SPSS software, with differences among groups being assessed via an analysis of variance followed by a Tukey's test and considered statistically significant when $p \leq 0.05$.

3. Results and discussion

3.1. Samples characterization

The typical XRD patterns of all samples were shown in Fig. 1a. It was evident that the main phases of the mineralized products for Ca^{2+} were $CaHPO_4 \cdot 2H_2O$ and $Ca_3(PO_4)_2$. The main reaction equations could be described as follows:

$$Ca^{2+} + HPO_4^{2-} + 2H_2O \leftrightarrow CaHPO_4 \cdot 2H_2O \qquad (1)$$

$$3Ca^{2+} + 2PO_4^{3-} + 2H_2O \leftrightarrow Ca_3(PO_4)_2 \qquad (2)$$

where Eq. (1) played a leading role during the reaction in acidic environments. With the increase of the pH values, part of the HPO_4^{2-} were converted to PO_4^{3-}, resulting in an increase of Eq. (2). Differing from Ca^{2+}, the main phases of the mineralized products for Sr^{2+} were

Table 1
ICP measured elemental composition of the synthesized samples.

pH	Ca			Sr		
	Ca (mol.%)	P (mol.%)	Ca:P	Sr (mol.%)	P (mol.%)	Sr:P
3.7	51.89 ± 1.05	48.11 ± 1.07	1.08 ± 0.07	55.71 ± 1.16	44.29 ± 1.00	1.26 ± 0.05
4.0	53.92 ± 1.08	46.08 ± 1.03	1.17 ± 0.08	56.42 ± 1.09	43.58 ± 0.98	1.29 ± 0.04
4.3	54.53 ± 0.97	45.47 ± 0.95	1.20 ± 0.04	57.08 ± 1.05	42.92 ± 0.96	1.33 ± 0.03
4.6	54.88 ± 1.12	45.12 ± 1.10	1.22 ± 0.09	58.38 ± 1.12	41.62 ± 0.99	1.40 ± 0.04
4.9	55.02 ± 0.89	44.98 ± 0.92	1.22 ± 0.06	59.02 ± 1.18	40.98 ± 1.03	1.44 ± 0.06
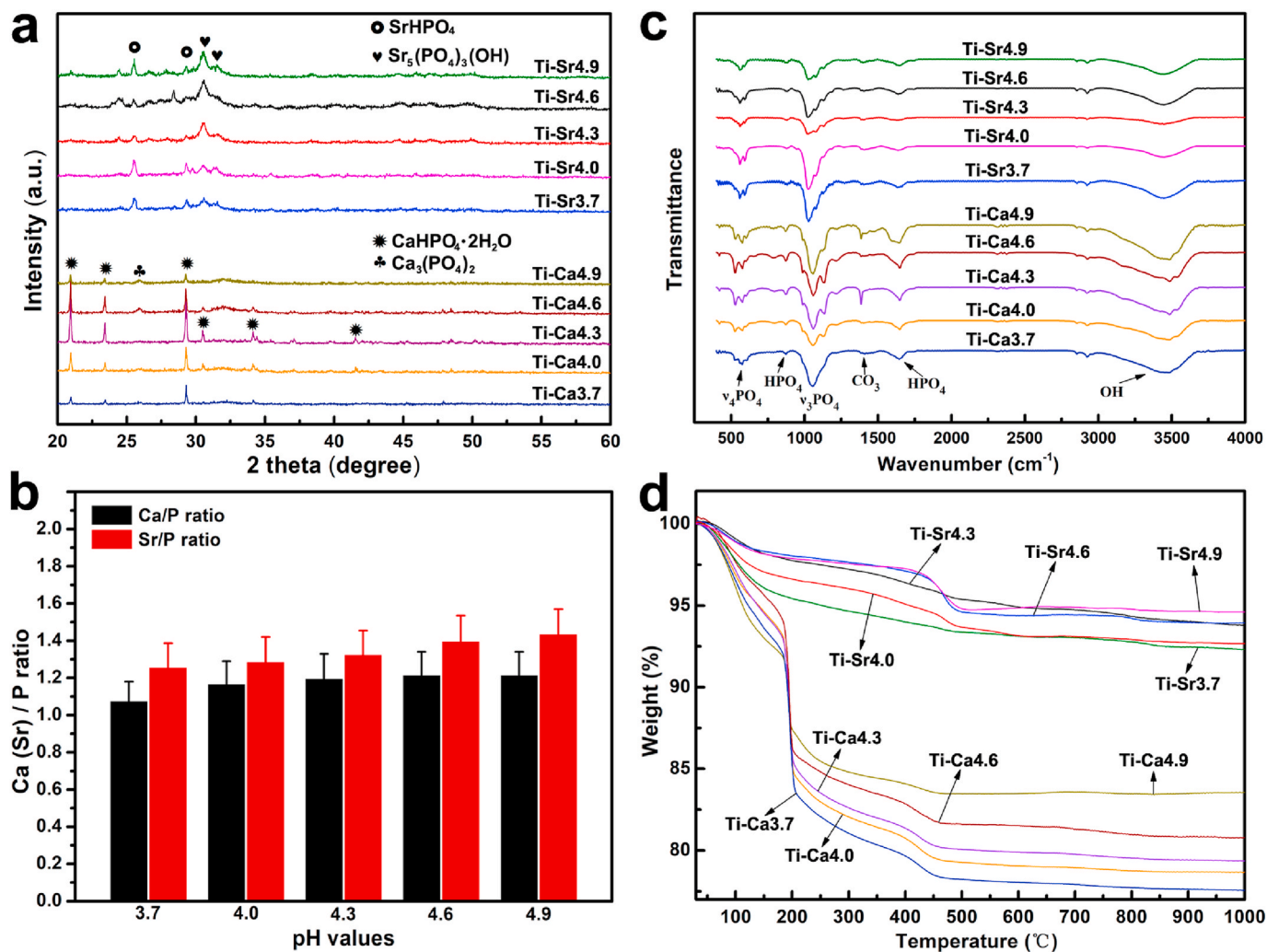
Fig. 1. (a) XRD patterns demonstrated that the main phases of the mineralized products for Ca^{2+} were $CaHPO_4 \cdot 2H_2O$ and $Ca_3(PO_4)_2$. Differing from Ca^{2+}, the main phases of the mineralized products for Sr^{2+} were $SrHPO_4$ and $Sr_5(PO_4)_3OH$. (b) ICP analysis showed the values of Sr:P were higher than those of Ca:P under the same acidic environment. (c) FT-IR spectra showed all samples were characteristic of phosphate compounds. (d) TG curves indicated Sr groups exhibited higher thermostability than Ca groups.

$$Sr^{2+} + HPO_4^{2-} \leftrightarrow SrHPO_4 \tag{3}$$

$$5Sr^{2+} + 3PO_4^{3-} + OH^- \leftrightarrow Sr_5(PO_4)_3OH \tag{4}$$

SrHPO$_4$ and Sr$_5$(PO$_4$)$_3$OH according to the following reaction equations:where Eq. (3) dominated the reactions at low pH environments (pH ≤ 4.3). Both the concentrations of PO_4^{3-} and OH^- increased with increasing of pH values (pH ≥ 4.3), which led to the formation of Sr$_5$(PO$_4$)$_3$OH according to Eq. (4). These results were confirmed by ICP analysis, as shown in Table 1 and Fig. 1b. Both the values of Ca:P and Sr:P increased with the increase of pH values. Meanwhile, it was worth noting that the values of Sr:P were higher than those of Ca:P under the same acidic environment. The FTIR spectra of all samples were characteristic of phosphate compounds which were in agreement with the XRD results, as shown in Fig. 1c. Meanwhile, it was worth noting that the HPO_4^{2-} intensities of Ca groups were stronger than those of Sr groups. TG analysis provided additional support for the results of XRD

and FTIR, as shown in Fig. 1d. Significant loss of weight up to approximately 200 °C for all samples was due to the loss of adsorbed water. There was a sudden weight loss at 200 °C for Ca groups which was due to the loss of crystal water [35]: $CaHPO_4 \cdot 2H_2O \rightarrow CaHPO_4 + H_2O$. HPO_4^{2-} accounted for the weight loss in the range of 400 °C–500 °C according to the following reaction [36]: $2HPO_4^{2-}O_4^{2-} \rightarrow P_2O_7^{4-} + H_2O$. It was apparent that Sr groups exhibited higher thermostability than Ca groups.

Fig. 2 a presented the typical SEM morphologies of all samples. For Ca groups, Ti-Ca3.7 showed a porous structure with a pore size of ~300 nm. This structure was changed into spherical as the pH values increased. Whereas for Sr groups, both Ti-Sr3.7 and Ti-Sr4.0 exhibited flake-like structure. With the increase of the pH.
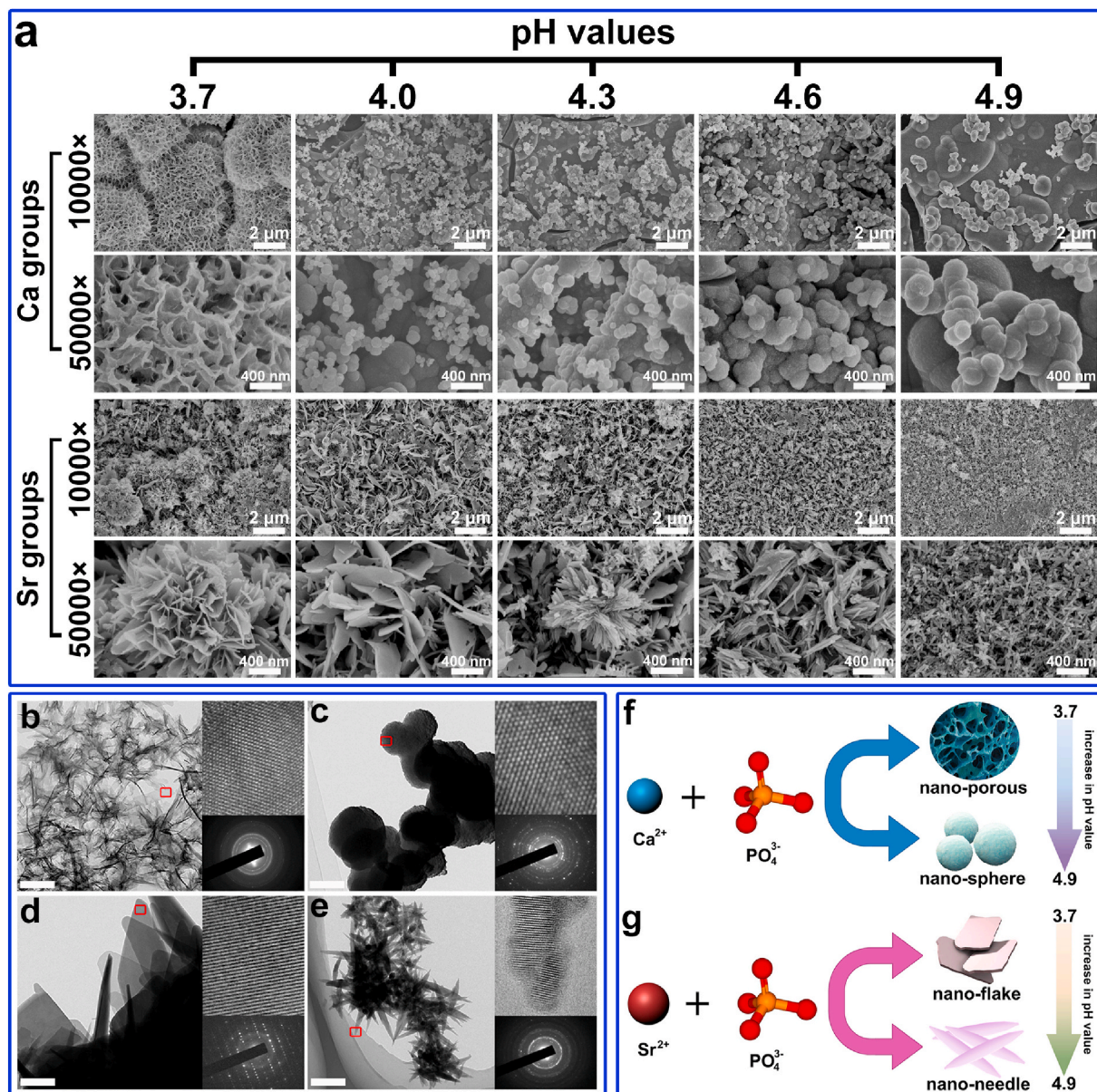

Fig. 2. (a) SEM images of the synthesized samples. With the increase of the pH values, the morphologies of Ca-groups were changed from porous to sphere structure. the morphologies of Sr-groups were changed from flake to needle structure. TEM images of the selected samples: (b) Ti-Ca3.7, (c) Ti-Ca4.9, (d) Ti-Sr3.7, and (e) Ti-Sr4.9. Schematic illustrating the mineralization behavior of: (f) Ca and (g) Sr.

Values, the morphology was changed from flake to needle structure. The aforementioned four typical structures were further confirmed and analyzed by TEM observation as shown in Fig. 2b–e. The results matched those from the SEM observation. Meanwhile, both the high resolution TEM (HRTEM) and selected area electron diffraction (SAED) images demonstrated all samples had good crystallinity. All these results indicated that Ca^{2+} and Sr^{2+} had different mineralization behaviors in acidic environments as schematic illustrated in Fig. 2f–g. The mineralized products for Ca^{2+} were $CaHPO_4 \cdot 2H_2O$ and $Ca_3(PO_4)_2$. In addition, the structure turned from nano-porous into nano-sphere with increasing pH values. Being different from Ca^{2+}, the mineralized products for Sr^{2+} were $SrHPO_4$ and $Sr_5(PO_4)_3OH$. Meanwhile, the structure turned from nano-flake into nano-needle with increasing pH values.

3.2. MSCs adhesion, spreading, proliferation and osteogenic differentiation

MSCs initial adhesion and spreading are very important for subsequent proliferation and differentiation [37–38]. After culturing for 12 h, MSCs were stained with phalloidin and DAPI and observed via laser confocal microscopy, as shown in Fig. 3a. The results showed that MSCs exhibited good adhesion on all samples. In addition, it was found that Ti-Sr4.9 and Ti-Ca4.9 showed better MSCs spreading than Ti-Sr3.7 and Ti-Ca3.7, respectively. In order to clarify this phenomenon, expressions of ITG α5 and ITG β1 were measured, as shown in Fig. 3b–c. We found the expressions of both ITG α5 and ITG β1 on Ti-Sr4.9 and Ti-Ca4.9 were higher than that of Ti-Sr3.7 and Ti-Ca3.7, respectively.

Moreover, it could be seen that Ti-Sr4.9 exhibited better MSCs spreading and higher ITG α5 and ITG β1 expressions than any other group. As well known, ITG α5β1 played an important role in modulating cell adhesion and spreading [39]. These results demonstrated that the mineralized products fabricated at high pH condition with the presence of Sr, for example Ti-Sr4.9, were beneficial to ITG α5β1 expression and MSCs adhesion and spreading. MSCs grew well on all groups after culturing for 3 days (Fig. 3d). Unsurprisingly, both the MSCs proliferation and ALP activity results demonstrated that Ti-Sr4.9 and Ti-Ca4.9 showed higher MSCs proliferation and ALP activity than Ti-Sr3.7 and Ti-Ca3.7, respectively. Finally, we measured the expressions of osteogenesis-related genes, including Runx2, ALP, Col-I, and OCN, as shown in Fig. 3g–j. Similar with the results of MSCs proliferation, Ti-Sr4.9 and Ti-Ca4.9 showed higher osteogenesis-related gene expressions than Ti-Sr3.7 and Ti-Ca3.7, respectively. Furthermore, compared with Ca-contained samples, Sr-contained samples promoted the osteogenic differentiation of MSC.

3.3. Osteoclast differentiation and activity

After culturing for 3 and 5 days, we performed TRAP staining and quantitative analysis, as shown in Fig. 4a–c. The results showed that BMMCs differentiated well on Ti group. However, compared with Ti group, both the number of TRAP positive cells and TRAP activity were decreased on Ti-Ca3.7 and Ti-Ca4.9 groups, especially for Ti-Ca3.7. This result was consistent with previous study that calcium-deficient
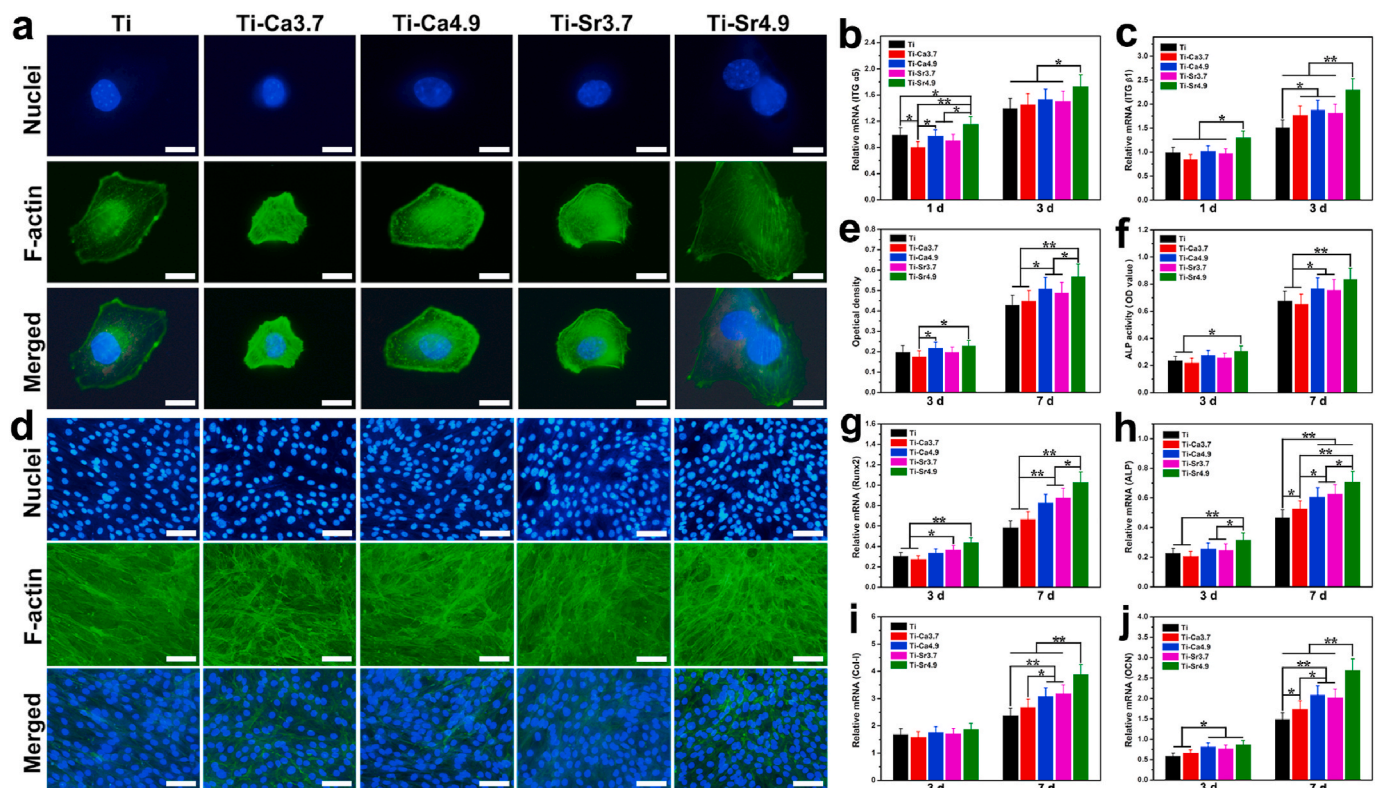

Fig. 3. (a) Representative confocal images of MSCs post seeding for 12 h, scale bars, 10 μm. Relative mRNA expression of (b) ITG α5 and (c) ITG β1 after culturing for 1 and 3 days on different samples. (d) Representative confocal images of MSCs after culturing for 3 days, scale bars, 50 μm. (e) MSCs proliferation on different samples measured by MTT assay. (f) ALP activity of MSCs after 3 and 7 days of incubation on each sample. Osteogenesis-related genes expression of MSC on different samples after culturing for 3 and 7 days: (g) Runx2, (h) ALP, (i) Col-I, and (j) OCN. Statistically significant differences, $*p < 0.05$ and $**p < 0.01$.
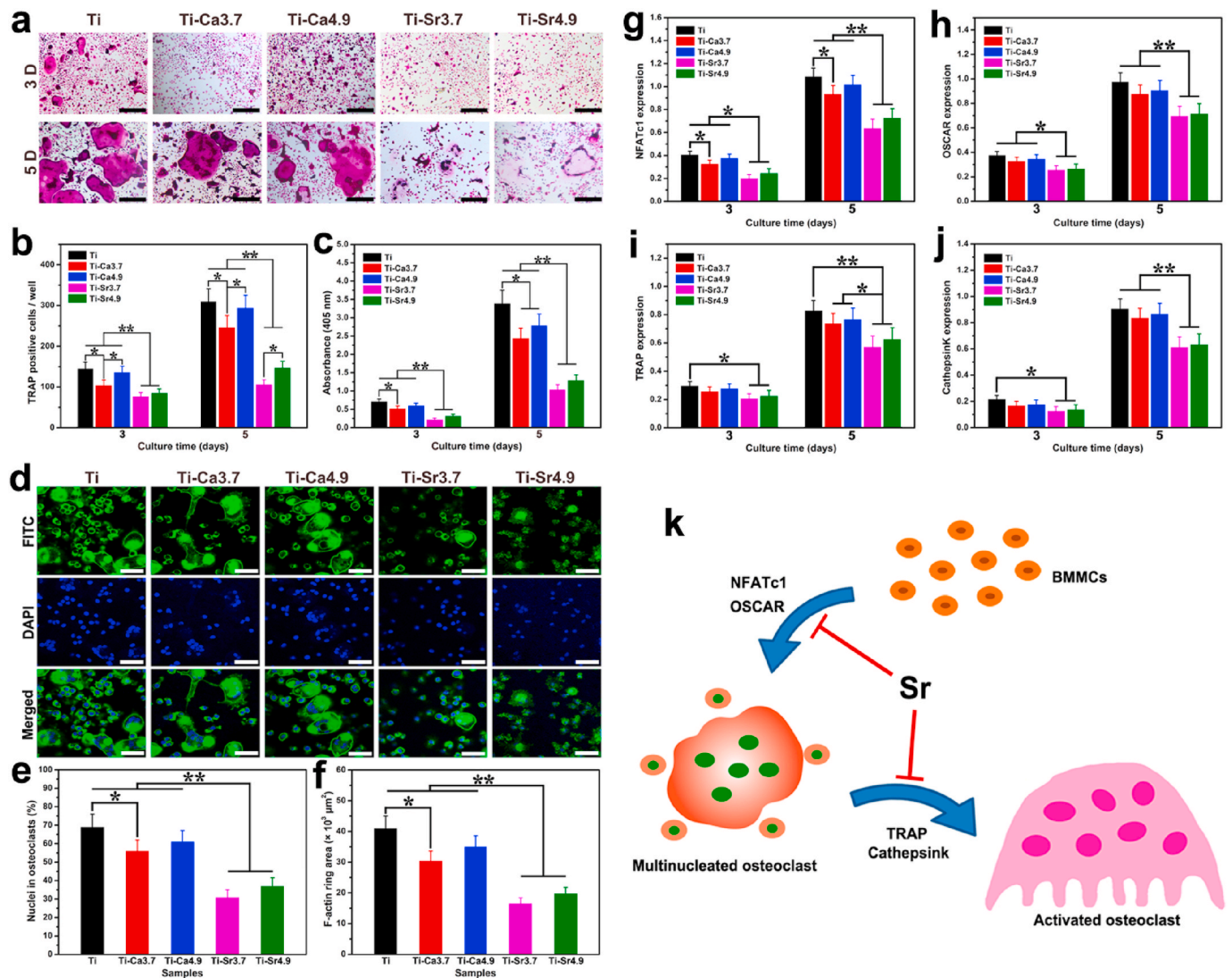
Fig. 4. (a) TRAP staining of osteoclasts after culturing for 3 and 5 days, scale bars, 400 μm. (b) Quantification of the number of TRAP-positive cell. (c) TRAP enzyme activity was measured at OD 405 nm. (d) Representative confocal images of differentiated osteoclasts immunostained for F-actin (green) and cell nuclei (blue), scale bar, 200 μm. (e) Quantification of the F-actin ring area and (f) % nuclei in osteoclasts. Osteoclastic genes expressions after culturing for 3 and 5 days: (g) NFATc1, (h) OSCAR, (i) TRAP, (j) Cathepsin K. (k) Schematic illustrating the effect of Sr on osteoclast differentiation. Statistically significant differences, $*p < 0.05$ and $**p < 0.01$.

apatite was unfavorable for osteoclast differentiation [40]. Moreover, both Ti-Sr3.7 and Ti-Sr4.9 groups showed significantly reduced TRAP positive cells and TRAP activity than other groups. Then, we performed immunofluorescence staining to evaluate the F-actin ring area and % nuclei in osteoclasts, as shown in Fig. 4d–f. Consistent with the TRAP staining results, both Ti-Sr3.7 and Ti-Sr4.9 groups showed significantly decreased F-actin ring area and % nuclei in osteoclasts than other groups. Finally, we investigated the expression of osteoclastogenesis-related genes, as shown in Fig. 4g–j. As well known, NFATc1 and OSCAR played important roles in regulating intracellular fusion [41]. Whereas for TRAP and Cathepsin K, they were involved in osteoclast activation [42]. The results demonstrated that Sr-substituted apatite coatings apparently inhibited the expressions of these osteoclastogenesis-related genes. In a word, Sr-substituted apatite coating suppressed

BMMCs fusion and osteoclast activity through inhibiting the expression of NFATc1, OSCAR, TRAP, and Cathepsin K, as schematically illustrated in Fig. 4k.

3.4. In vivo evaluation of the bone-implant condition

At each point of time, we first performed X-ray, a simple and commonly used clinical detection method, to quickly get an observation of the implant condition, as shown in Fig. 5a. It could be seen that all implants showed good biocompatibility with surrounding bone tissues. Then, we performed a push-in test to evaluate the bone-implant bonding strength, as shown in Fig. 5a. The results showed that both Ca-contained groups and Sr-contained groups could significantly promote the bone-implant bonding strength when compared with Ti group. In
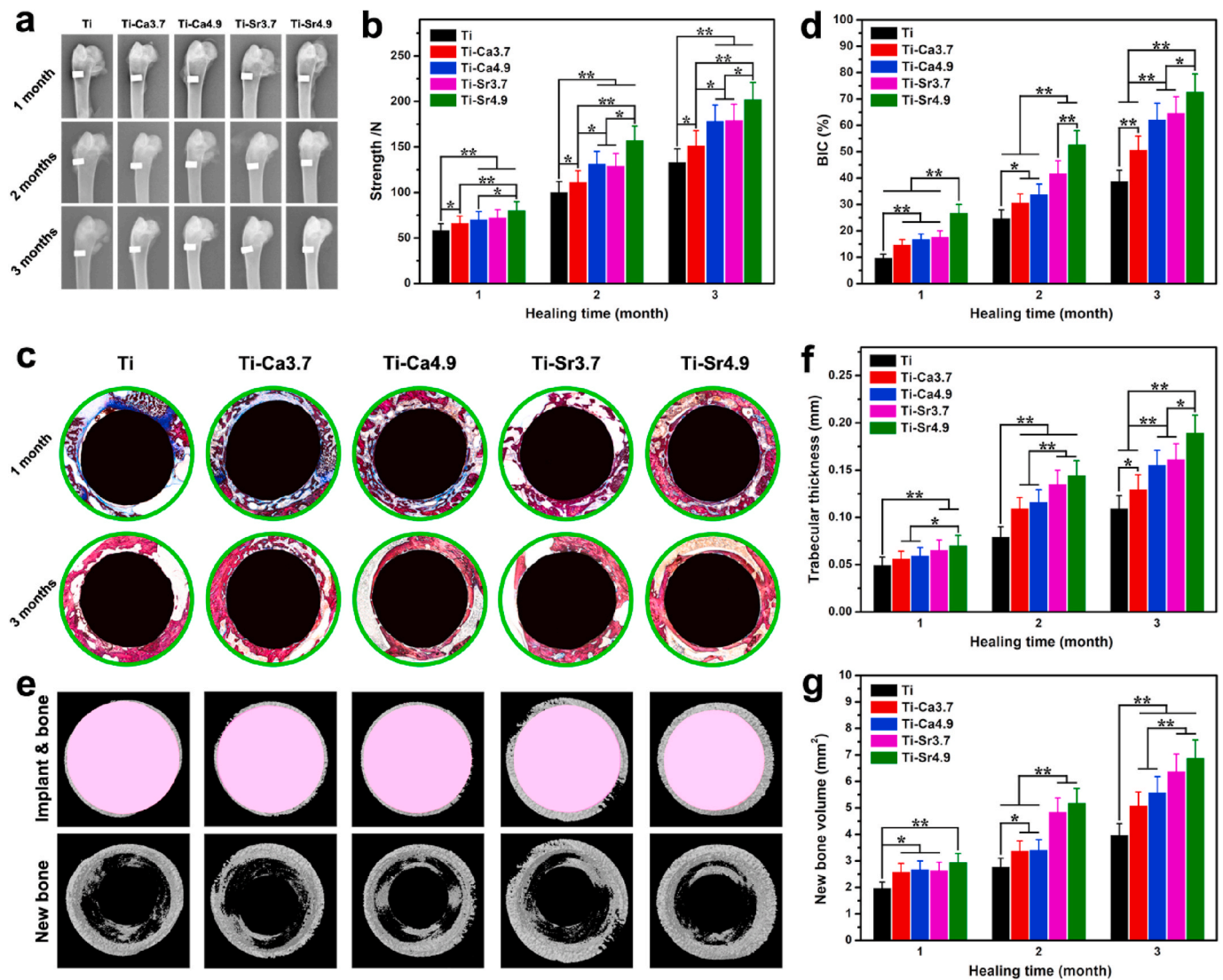
Fig. 5. (a) X-ray observation of the implant conditions. (b) Bone-implant bonding strength measured by a push-in test. (c) Undecalcified histological observations of the bone-implant interface. (d) Bone-implant contact (BIC) values at each harvest time. (e) Micro-CT images of the implant & surrounding new bone 2 months post-surgery. Quantitative analysis of: (f) trabecular thickness and (g) new bone volume. Statistically significant differences, *$p < 0.05$ and **$p < 0.01$ shown in Fig. 5c–d and Fig. S1a. It was obvious that BIC values increased over time for all groups. In addition, Ti-Sr4.9 and Ti-Ca4.9 showed higher BIC values than Ti-Sr3.7 and Ti-Ca3.7, respectively. Moreover, Ti-Sr4.9 exhibited the highest BIC values throughout the experiment. Finally, we performed micro-CT scan to investigate the trabecular thickness and new bone volume surrounding implant, as shown in Fig. 5e–g and Fig. S1b. The results showed that both the trabecular thickness and new bone volume increased over time for all groups. In addition, both Ca-contained groups and Sr-contained groups could significantly promote the trabecular thickness and new bone volume when compared with Ti group. Moreover, Sr-contained groups, especially for Ti-Sr4.9 group, showed higher trabecular thickness and new bone volume than other groups.

addition, the bone-implant bonding strength of Ti-Ca4.9 was comparable with that of Ti-Sr3.7, which was higher than that of Ti-Ca3.7. Moreover, Ti-Sr4.9 exhibited the highest bonding strength throughout the experiment. Undecalcified bone slicing accompanied by BIC analysis were conducted to further explore the bone-implant interface, as.

3.5. Histological analysis

After 1, 2, and 3 months of implantation, we performed decalcified histological analysis via HE and Masson's trichrome staining to gain more information of the new formed bone, as shown in Fig. 6. At 1 month post-implantation, there were many gaps accompanied with rare new bone formed (black arrows) around Ti group. In addition, although the gaps were decreased when compared with Ti group, only a few bone formed in Ti-Ca3.7, Ti-Ca4.9, and Ti-Sr3.7 groups. Moreover, Ti-Sr4.9 group exhibited apparent more new bone than other groups. At 2

months post-operation, all groups showed obvious increased new bone formation, especially for Ti-Sr4.9 group. At 3 months post-surgery, there were still lots of gaps in the new bone for Ti group. At the meantime, new bone around Ti-Sr4.9 exhibited dense structure, which was similar with mature bone. All these results indicated that Sr-contained samples, especially for Ti-Sr4.9 group, were in favor of bone formation and maturation.

3.6. TRAP and immunohistochemical analysis

In order to understand the underlying mechanism of the effect of coatings on new bone growth, TRAP and immunohistochemical staining were performed, as shown in Fig. 7. It was evident that both Ti-Ca3.7 and Ti-Ca4.9 showed comparable N. TRAP$^+$ with Ti. Whereas for Sr-contained coatings, both Ti-Sr3.7 and Ti-Sr4.9 showed significantly decreased N. TRAP$^+$ compared with other groups (Fig. 7a–b). The
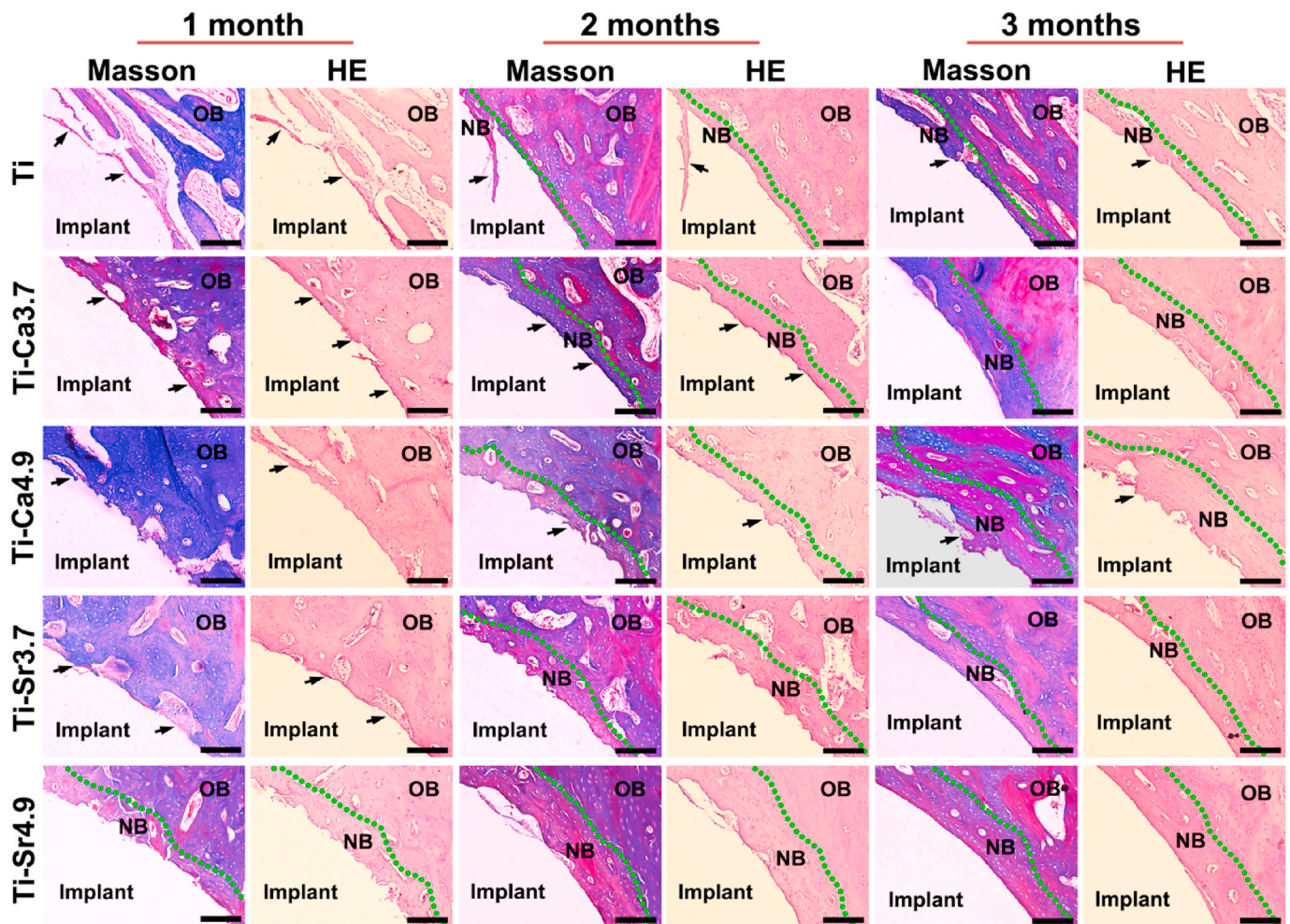
Fig. 6. Histological analysis by HE and Masson's trichrome staining after 1, 2, and 3 months of implantation. The results indicated that Sr-contained samples, especially for Ti-Sr4.9 group, were in favor of bone formation and maturation. OB, old bone; NB, new bone; black arrow, new bone; green dotted line, the interface between OB and NB. Scale bars, 400 μm.

results of immunohistochemical staining revealed that both the Ca-coatings and Sr-coatings could significantly promote the expressions of Col-I and OCN. Moreover, Sr-coatings, especially for Ti-Sr4.9, showed significantly higher N. Col-I$^+$ and N. OCN$^+$ than Ca-coatings (Fig. 7c–f). All these results demonstrated that the Sr-coatings, especially for Ti-Sr4.9, accelerated *in vivo* bone formation through promoting the expressions of Col-I and OCN and suppressing osteoclast activity.

Sr, an element located in the same main group with Ca, has gained wide concern in recent years. Due to its good biocompatibility and similarity with Ca, Sr was generally incorporated into bone filling materials and implant coatings [43–45]. In addition, because of its anti-osteoclast property, Sr also had applications in the field of drugs. For example, strontium ranelate, an anti-osteoporosis drug, has achieved remarkable clinical success in reducing the risk of fracture of post-menopausal women [46]. Therefore, Sr-contained biomaterials have a good clinical application prospect. Based on this, we fabricated a series of apatite and Sr-substituted apatite coatings in this study. Our findings found that Ca^{2+} and Sr^{2+} showed different mineralization behaviors. The *in vitro* study revealed that Sr-substituted coating could regulate

MSCs adhesion and osteogenic differentiation through promoting the expression of ITG α5β1, ALP, Runx2, OCN, and Col-I. In addition, Sr-substituted coating inhibited osteoclast differentiation and activity through suppressing the expression of NFATc1, OSCAR, TRAP, and Cathepsin K. What's more, we found that nano-needle Sr-substituted coating fabricated at high pH condition showed optimal biological performance, as illustrated in Fig. 8. All these features gave it better *in vivo* performances, such as suppressing osteoclastic activity, promoting bone formation and osseointegration. Above all, this study offered a Sr-substituted apatite coating with promising application for treatment of osteoporotic patients and might provide a basic reference for implant coating design.

4. Conclusion

In this study, a series of apatite and Sr-substituted apatite coatings were fabricated via electrochemical deposition. The results indicated that Ca^{2+} and Sr^{2+} showed different mineralization behaviors. The *in vitro* experiment revealed that nano-needle Sr-substituted apatite coating fabricated at high pH condition exhibited optimal
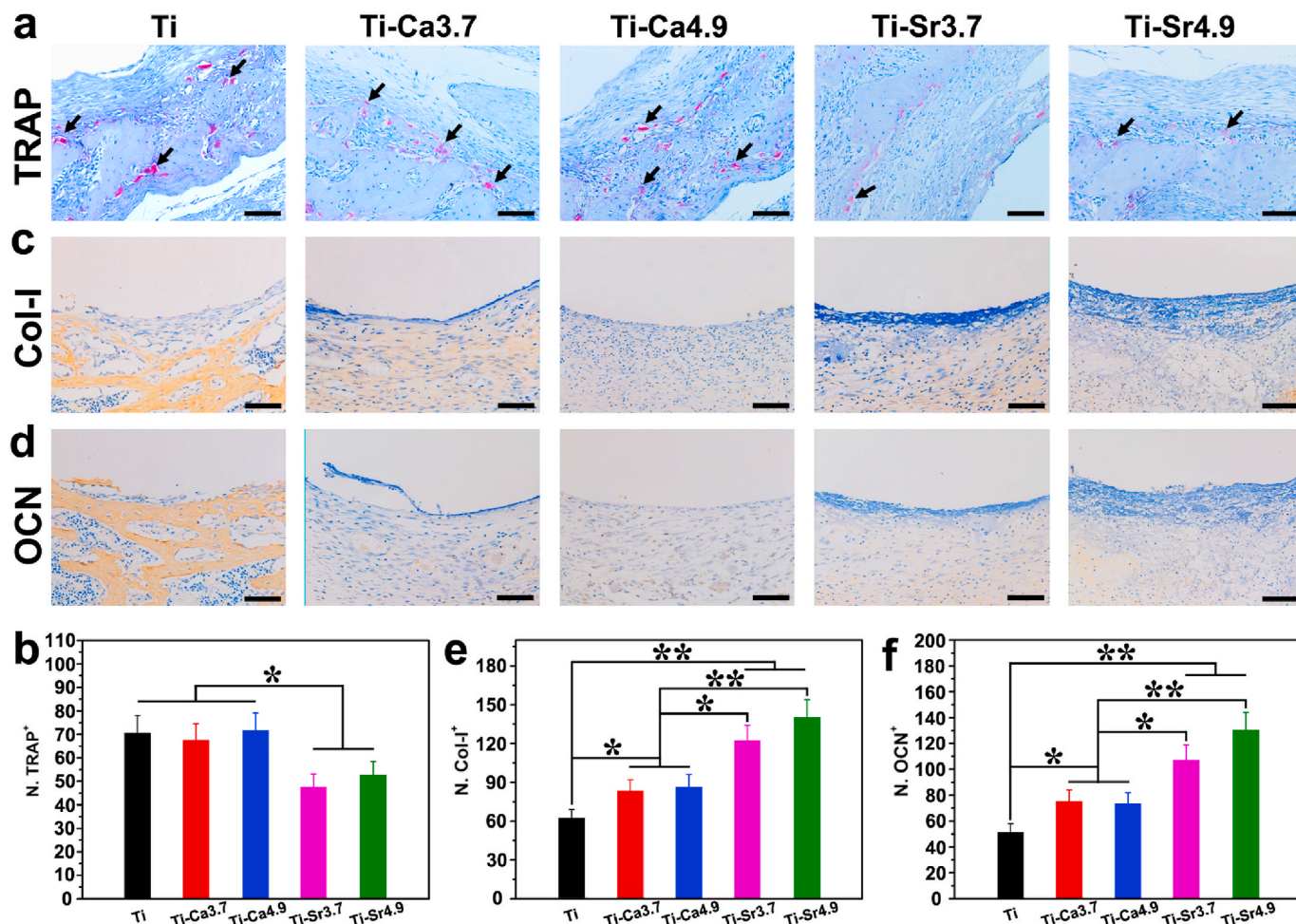
Fig. 7. TRAP and immunohistochemical staining were performed after implantation for 14 days. (a) TRAP staining and (b) quantitative analysis. (c–d) Immunohistochemical staining and (e–f) quantification of positive cells. The results showed that the Sr-coatings, especially for Ti-Sr4.9, promoted the expressions of Col-I and OCN and suppressed the expression of TRAP *in vivo*. Scale bars, 200 μm. Statistically significant differences, *$p < 0.05$ and **$p < 0.01$.
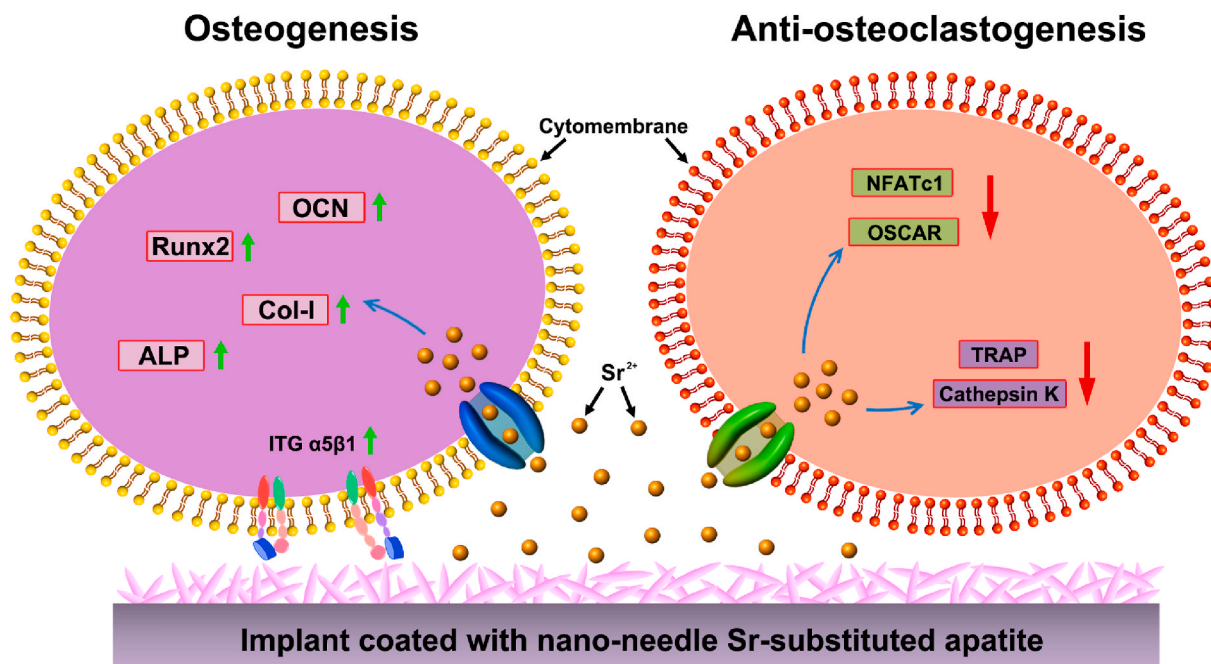

Fig. 8. Schematic illustrating the effect of nano-needle Sr-substituted apatite on promoting osteogenesis and inhibiting osteoclastogenesis.

comprehensive properties in promoting MSCs adhesion, spreading, proliferation, and osteogenic differentiation and inhibiting osteoclast differentiation and fusion. In addition, the *in vivo* study demonstrated that nano-needle Sr-substituted apatite coating suppressed osteoclastic activity, promoted new bone formation, and improved bone-implant integration. It was believed that the bifunctional Sr-substituted coating might have potential clinical applications.

CRediT authorship contribution statement

Zhen Geng: Conceptualization, Methodology, Formal analysis, Investigation, Writing - original draft. **Luli Ji:** Methodology, Formal analysis. **Zhaoyang Li:** Supervision, Writing - review & editing. **Jing Wang:** Formal analysis. **Hongyan He:** Conceptualization, Supervision. **Zhenduo Cui:** Conceptualization, Methodology, Supervision. **Xianjin Yang:** Supervision. **Changsheng Liu:** Supervision, Funding acquisition.

Declaration of competing interest

The authors declare that they have no known competing financial interests or personal relationships that could have appeared to influence the work reported in this paper.

Acknowledgement

Appendix A. Supplementary data

Supplementary data to this article can be found online at https://doi.org/10.1016/j.bioactmat.2020.09.024.

References

[1] D.J. Hunter, B.Z. Sita, Osteoarthritis, Lancet 393 (2019) 1745–1759.
[2] S. Glyn-Jones, A.J.R. Palmer, R. Agricola, A.J. Price, T.L. Vincent, H. Weinans, A.J. Carr, Osteoarthritis, Lancet 386 (2015) 376–387.
[3] C. Hu, D. Ashok, D.R. Nisbet, V. Gautam, Bioinspired surface modification of orthopedic implants for bone tissue engineering, Biomaterials 219 (2019) 119366.
[4] G.I. Im, M.K. Kim, The relationship between osteoarthritis and osteoporosis, J. Bone Miner. Metabol. 32 (2014) 101–109.
[5] B. Ghosh, T. Pal, S. Ganguly, A. Ghosh, A study of the prevalence of osteoporosis and hypovitaminosis D in patients with primary knee osteoarthritis, J. Clin. Orthop. Trauma. 5 (2014) 199–202.
[6] M. Miyashita, T. Ogawa, H. Naito, A. Shibamoto, A.S. Wang, K. Shobara, K. Sasaki, Evaluation of implant screw loosening by resonance frequency analysis with triaxial piezoelectric pick-up: in vitro model and in vivo animal study, Clin. Oral Invest. 22 (2018) 2129–2134.
[7] D. Apostu, O. Lucaciu, C. Berce, D. Lucaciu, D. Cosma, Current methods of preventing aseptic loosening and improving osseointegration of titanium implants in cementless total hip arthroplasty: a review, J. Int. Med. Res. 46 (2018) 2104–2119.
[8] D.B. Raina, D. Larsson, E.A. Sezgin, H. Isaksson, M. Tagil, L. Lidgren, Biomodulation of an implant for enhanced bone-implant anchorage, Acta Biomater. 96 (2019) 619–630.
[9] B. Mavcic, V. Antolic, V. Dolzan, Association of NLRP3 and CARD8 inflammasome polymorphisms with aseptic loosening after primary total hip arthroplasty, J. Orthop. Res. 38 (2020) 417–421.
[10] S.S. Mehdi, M.T. Khorasani, D.K. Ehsan, J. Ahmad, Synthesis methods for nanosized hydroxyapatite with diverse structures, Acta Biomater. 9 (2013) 7591–7621.
[11] X. Zhang, J.B. Fan, C.S. Lee, S. Kim, C. Chen, T. Aghaloo, M. Lee, Apatite-binding nanoparticulate agonist of hedgehog signaling for bone repair, Adv. Funct. Mater. 30 (2020) 1909218.
[12] X.F. Li, T. Song, X.N. Chen, M.L. Wang, X. Yang, Y.M. Xiao, X.D. Zhang, Osteoinductivity of porous biphasic calcium phosphate ceramic spheres with nanocrystalline and their efficacy in guiding bone regeneration, ACS Appl. Mater. Interfaces 11 (2019) 3722–3736.
[13] D. Arcos, M. Vallet-Regi, Substituted hydroxyapatite coatings of bone implants, J. Mater. Chem. B 8 (2020) 1781–1800.
[14] C.C. Wang, Z.B. Fan, Y. Han, Formation and osteoblast behavior of HA nano-rod/ fiber patterned coatings on tantalum in porous and compact forms, J. Mater. Chem. B 3 (2015) 5442–5454.
[15] J.L. Moreau, H.H.K. Xu, Mesenchymal stem cell proliferation and differentiation on an injectable calcium phosphate - chitosan composite scaffold, Biomaterials 30 (2009) 2675–2682.
[16] Y.L. Cheng, Y.W. Chen, K. Wang, M.Y. Shie, Enhanced adhesion and differentiation of human mesenchymal stem cell inside apatite-mineralized/poly(dopamine)-coated poly(ecaprolactone) scaffolds by stereolithography, J. Mater. Chem. B 4 (2016) 6307–6315.
[17] R. Zhou, D.Q. Wei, J.Y. Cao, W. Feng, S. Cheng, Q. Du, B.Q. Li, Y.M. Wang, D.C. Jia, Y. Zhou, Synergistic effects of surface chemistry and topologic structure from modified microarc oxidation coatings on Ti implants for improving osseointegration, ACS Appl. Mater. Interfaces 7 (2015) 8932–8941.
[18] T. Kokubo, S. Yamaguchi, Novel bioactive materials developed by simulated body fluid evaluation: surface-modified Ti metal and its alloys, Acta Biomater. 44 (2016) 16–30.
[19] Y. Gao, S.J. Zou, X.G. Liu, C.Y. Bao, J. Hu, The effect of surface immobilized bisphosphonates on the fixation of hydroxyapatite-coated titanium implants in ovariectomized rats, Biomaterials 30 (2008) 1790–1796.
[20] B. Reynard, V. Balter, Trace elements and their isotopes in bones and teeth: diet, environments, diagenesis, and dating of archeological and paleontological samples, Palaeogeogr. Palaeocl. 416 (2014) 4–16.
[21] X. Cui, Y.D. Zhang, J.Y. Wang, C.C. Huang, Y.D. Wang, H.S. Yang, W.L. Liu, T. Wang, D.P. Wang, G.C. Wang, C.S. Ruan, D.F. Chen, W.W. Lu, W.H. Huang, M.N. Rahaman, H.B. Pan, Strontium modulates osteogenic activity of bone cement composed of bioactive borosilicate glass particles by activating Wnt/beta-catenin signaling pathway, Bioact. Mater. 5 (2020) 334–347.
[22] C. Zhou, A.T. Xu, D.D. Wang, G.F. Lin, T. Liu, F.M. He, The effects of Sr-incorporated micro/nano rough titanium surface on rBMSC migration and osteogenic differentiation for rapid osteointegration, Biomater. Sci. 6 (2018) 1946–1961.
[23] P. Naruphontjirakul, O. Tsigkou, S.W. Li, A.E. Porter, J.R. Jones, Human mesenchymal stem cells differentiate into an osteogenic lineage in presence of strontium containing bioactive glass nanoparticles, Acta Biomater. 90 (2019) 373–392.
[24] B. Kruppke, A.S. Wagner, M. Rohnke, C. Heinemann, C. Kreschel, A. Gebert, H.P. Wiesmann, S. Mazurek, S. Wenisch, T. Hanke, Biomaterial based treatment of osteoclastic/osteoblastic cell imbalance - gelatin-modified calcium/strontium phosphates, Mater. Sci. Eng. C 104 (2019) 109933.
[25] H. Xie, Q. Ye, Strontium: friend or foe of bone formation? Osteoporos. Int. 26 (2015) 2213–2214.
[26] H.X. Xie, Z.P. Gu, Y. He, J. Xu, C. Xu, L.J. Li, Q.S. Ye, Microenvironment construction of strontium–calcium-based biomaterials for bone tissue regeneration: the equilibrium effect of calcium to strontium, J. Mater. Chem. B 6 (2018) 2332–2339.
[27] S. Ray, U. Thormann, M. Eichelroth, M. Budak, C. Biehl, M. Rupp, U. Sommer, T. El Khassawna, F.I. Alagboso, M. Kampschulte, M. Rohnke, A. Henß, K. Peppler, V. Linke, P. Quadbeck, A. Voigt, F. Stenger, D. Karl, R. Schnettler, C. Heiss, K.S. Lips, V. Alt, Strontium and bisphosphonate coated iron foam scaffolds for osteoporotic fracture defect healing, Biomaterials 157 (2018) 1–16.
[28] M. Pilmane, K. Salma-Ancane, D. Loca, J. Locs, L. Berzina-Cimdina, Strontium and strontium ranelate: historical review of some of their functions, Mater. Sci. Eng. C 78 (2017) 1222–1230.
[29] L. Weng, S.K. Boda, M.J. Teusink, F.D. Shuler, X.R. Li, J.W. Xie, Binary doping of strontium and copper enhancing osteogenesis and angiogenesis of bioactive glass nanofibers while suppressing osteoclast activity, ACS Appl. Mater. Interfaces 9 (2017) 24484–24496.
[30] J.K. Zeng, J.S. Guo, Z.Y. Sun, F.Y. Deng, C.Q. Ning, Y.Z. Xie, Osteoblastic and antiosteoclastic activities of strontium-substituted silicocarnotite ceramics: in vitro and in vivo studies, Bioact. Mater. 5 (2020) 435–446.
[31] M.A.E. Cruz, C.B. Tovani, B.Z. Favarin, M.P.R. Soares, S.Y. Fukada, P. Ciancaglini, A.P. Ramos, Synthesis of Sr-morin complex and its in vitro response: decrease in osteoclast differentiation while sustaining osteoblast mineralization ability, J. Mater. Chem. B 7 (2019) 823–829.
[32] X.M. Luo, D. Barbieri, R.Q. Duan, H.P. Yuan, J.D. Bruijn, Strontium-containing apatite/polylactide composites enhance bone formation in osteopenic rabbits, Acta Biomater. 26 (2015) 331–337.
[33] L.X. Mao, L.G. Xia, J. Chang, J.Q. Liu, L.Y. Jiang, C.T. Wu, B. Fang, The synergistic effects of Sr and Si bioactive ions on osteogenesis, osteoclastogenesis and angiogenesis for osteoporotic bone regeneration, Acta Biomater. 61 (2017) 217–232.
[34] D.Z. Li, K.W. Chen, L. Duan, T.W. Fu, J. Li, Z.X. Mu, S. Wang, Q. Zou, L. Chen, Y.Y.F. Feng, Y.H. Li, H.M. Zhang, H.A. Wang, T. Chen, P. Ji, Strontium ranelate incorporated enzyme-cross-linked gelatin nanoparticle/silk fibroin aerogel for osteogenesis in OVX-induced osteoporosis, ACS Biomater. Sci. 5 (2019) 1440–1451.
[35] F. Ren, Y. Leng, R. Xin, X. Ge, Synthesis, characterization and ab initio simulation of magnesium-substituted hydroxyapatite, Acta Biomater. 6 (2010) 2787–2796.
[36] S. Kannan, I.A.F. Lemos, J.H.G. Rocha, J.M.F. Ferreira, Synthesis and characterization of magnesium substituted biphasic mixtures of controlled hydroxyapatite/β-tricalcium phosphate ratios, J. Solid State Chem. 178 (2005) 3190–3196.
[37] H.P. Felgueiras, M.D.M. Evans, V. Migonney, Contribution of fibronectin and vitronectin to the adhesion and morphology of MC3T3-E1 osteoblastic cells to poly (NaSS) grafted Ti6Al4V, Acta Biomater. 28 (2015) 225–233.
[38] Y.D. Cui, F.M. Hameed, B. Yang, K. Lee, C.Q. Pan, S. Park, M. Sheetz, Cyclic stretching of soft substrates induces spreading and growth, Nat. Commun. 6 (2015) 6333.
[39] Y.L. Yu, X.K. Shen, Z. Luo, Y. Hu, M.H. Li, P.P. Ma, Q.C. Ran, L.L. Dai, Y. He, K.Y. Cai, Osteogenesis potential of different titania nanotubes in oxidative stress

microenvironment, Biomaterials 167 (2018) 44–57.

[40] Y. Shiwaku, K. Tsuchiya, L. Xiao, O. Suzuki, Effect of calcium phosphate phases affecting the crosstalk between osteoblasts and osteoclasts in vitro, J. Biomed. Mater. Res. 107 (2019) 1001–1013.

[41] T. Negishi-Koga, H. Takayanagi, Ca^{2+}-NFATc1 signaling is an essential axis of osteoclast differentiation, Immunol. Rev. 231 (2009) 241–256.

[42] T.R. Arnett, I.R. Orriss, Metabolic properties of the osteoclast, Bone 115 (2018) 25–30.

[43] M.R. Shahrouzifar, E. Salahinejad, E. Sharifi, Co-incorporation of strontium and fluorine into diopside scaffolds: bioactivity, biodegradation and cytocompatibility evaluations, Mater. Sci. Eng. C 103 (2019) 109752.

[44] Z.S. Tao, W.S. Zhou, X.W. He, W. Liu, B.L. Bai, Q. Zhou, Z.L. Huang, K.K. Tu, H. Li,

T. Sun, Y.X. Lv, W. Cui, L. Yang, A comparative study of zinc, magnesium, strontium-incorporated hydroxyapatite-coated titanium implants for osseointegration of osteopenic rats, Mater. Sci. Eng. C 62 (2016) 226–232.

[45] V. Offermanns, O.Z. Andersen, G. Riede, M. Sillassen, C.S. Jeppesen, K.P. Almtoft, H. Talasz, C. Ohman-Magi, B. Lethaus, R. Tolba, F. Kloss, M. Foss, Effect of strontium surface-functionalized implants on early and late osseointegration: a histological, spectrometric and tomographic evaluation, Acta Biomater. 69 (2018) 385–394.

[46] M. Pilmane, K. Salma-Ancane, D. Loca, J. Locs, L. Berzina-Cimdina, Strontium and strontium ranelate: historical review of some of their functions, Mater. Sci. Eng. C 78 (2017) 1222–1230.